

# Reversible Sodiation of Electrochemically Deposited Binder- and Conducting Additive-Free Si–O–C Composite Layers

Steffen Link, Anna Dimitrova, Stefan Krischok, and Svetlozar Ivanov\*

Binder- and conducting additive-free Si–O–C composite layers are deposited electrochemically under potentiostatic conditions from sulfolane-based organic electrolyte. Quartz crystal microbalance with damping monitoring is used for evaluation of the layer growth and its physical properties. The sodiation–desodiation performance of the material is afterward explored in Na-ion electrolyte. In terms of specific capacity, rate capability, and long-term electrochemical stability, the experiments confirm the advantages of applying the electrochemically formed Si–O–C structure as anode for Na-ion batteries. The material displays high ( $722 \text{ mAh g}^{-1}$ ) initial reversible capacity at  $j = 70 \text{ mA g}^{-1}$  and preserves stable long-term capacity of  $540 \text{ mAh g}^{-1}$  for at least 400 galvanostatic cycles, measured at  $j = 150 \text{ mA g}^{-1}$ . The observed high performance can be attributed to its improved mechanical stability and accelerated Na-ion transport in the porous anode structure. The origin of the material electroactivity is revealed based on X-Ray photoelectron spectroscopic analysis of pristine (as deposited), sodiated, and desodiated Si–O–C layers. The evaluation of the spectroscopic data indicates reversible activity of the material due to the complex contribution of carbon and silicon redox centers.

## 1. Introduction

Li-ion batteries (LIBs) are still the most competitive electrochemical energy storage systems, owing to their long cycle life and outstanding functional performance of the applied active materials. However, the worldwide lithium resources cannot be considered as a long-term stable supply for the globally increasing LIB production.<sup>[1]</sup> Therefore, in recent years, a wide range of post-lithium chemistries has received a great deal of attention with the sodium-ion battery (SIB) being the most thoroughly studied emerging technology.<sup>[2]</sup>

Due to the large ionic radius of sodium, the materials known from the SIB research do not always operate identically, compared to their Li-ion counterparts.<sup>[3]</sup> To design well-functioning electrode materials for SIBs, the scientific knowledge related to the structural aspects of the sodiation

process (i.e., reaction mechanism, Na-ion transport phenomena and electrochemical–mechanical behavior related to these processes) has to be substantially enhanced.

Among many advanced materials, silicon has been also investigated as a possible anode in SIBs, motivated by its remarkable specific capacity in Li electrolytes. However, it turned out that the sodiation of the crystalline Si phase is kinetically and thermodynamically unfavorable, which has been confirmed by first principle *ab initio* calculations.<sup>[4,5]</sup> In contrast to that, the computational studies have revealed the ability of the amorphous Si phase to provide a theoretical capacity of  $724 \text{ mAh g}^{-1}$  during redox reaction with sodium.<sup>[4]</sup> Nevertheless, the experimental works on the sodiation of amorphous silicon have shown much lower specific capacity values.<sup>[6–9]</sup> Additionally, the reversible sodium-ion uptake of 20 nm silicon nanoparticles with a mixed (amorphous and crystalline) structure has been demonstrated, yielding a capacity retention (CR) of only  $248 \text{ mAh g}^{-1}$  in 100 galvanostatic cycles.<sup>[10]</sup>

Next to the pure Si phase, different Si-containing compounds, displaying improved mechanical stability upon sodiation have been explored.<sup>[11–16]</sup> Shimizu et al.<sup>[11]</sup> tested electrochemically silicon oxide (SiO) phase in Na<sup>+</sup>-containing electrolyte and suggested that the sodiation of this structure is governed by a conversion-alloying-based reaction, where the in situ formed nanosized silicon domains can reversibly alloy with sodium.<sup>[11]</sup> Recently, the electrochemical performance of nanosized silicon

S. Link

Institute for Sensor and Actuator Technology  
Hochschule für Angewandte Wissenschaften Coburg  
96450 Coburg, Germany

A. Dimitrova, S. Krischok

Institute of Physics and Institute of Micro- and Nanotechnologies  
MacroNano  
Technische Universität Ilmenau  
98693 Ilmenau, Germany


A. Dimitrova

Department for Research and Development  
IBU-Tec Advanced Materials AG  
99425 Weimar, Germany

S. Ivanov

Electrochemistry and Electroplating Group  
Technische Universität Ilmenau  
98693 Ilmenau, Germany

E-mail: svetlozar-dimitrov.ivanov@tu-ilmenau.de

 The ORCID identification number(s) for the author(s) of this article can be found under <https://doi.org/10.1002/ente.202101164>.

© 2022 The Authors. Energy Technology published by Wiley-VCH GmbH. This is an open access article under the terms of the Creative Commons Attribution-NonCommercial-NoDerivs License, which permits use and distribution in any medium, provided the original work is properly cited, the use is non-commercial and no modifications or adaptations are made.

DOI: 10.1002/ente.202101164

oxycarbide anodes in sodium-based electrolytes has also been studied.<sup>[12,14,16]</sup> This approach resulted in an improvement of the cycling stability of the material at low capacity values and limited electrochemical activity of the silicon component, yielding a specific capacity in the range of 160–180 mAh g<sup>-1</sup>.<sup>[14,16]</sup> It was shown that the electrochemical stability of the Si-based anodes for SIB can be achieved by integrating the active Si component in a suitable, mechanically stable structure.<sup>[11–16]</sup>

Synthesis and deposition techniques play a central role for tuning the functional behavior of the battery materials, where the electrochemical methods encompass an underexplored subject in this field. Electrodeposition is a simple and versatile method, which arouses great interests of battery researchers. It can be applied for the formation of many active and inactive components of the batteries. As compared to the conventional deposition technologies, the advantages of this approach provide multiple benefits, for example, enhancing battery performance and enabling assembly of batteries with new architecture that conventional technologies are unable to fabricate.<sup>[17]</sup> Along with other effective methods, silicon-containing materials have been deposited also electrochemically, at room temperature, in different organic-based electrolytes.<sup>[18–23]</sup> The analysis of their chemical composition showed that apart from elemental silicon, depending on the electrolyte type, the deposits typically contain considerable amounts of additional components, originating from the decomposition of the corresponding solvent and supporting electrolyte salt.<sup>[20–23]</sup> According to the authors' knowledge, the sodiation behavior of this type of silicon-containing composite materials has not been explored so far.

The electrochemical deposition method was further developed in terms of improved applicability of the Si–O–C-based materials for electrochemical energy storage. In this context, Ahn et al. demonstrated the electrochemical formation and application of powdered Si–O–C composite for LIB anode, where a specific discharge capacity of 616 mAh g<sup>-1</sup> and an impressive cycling stability (over 10 000 cycles) have been shown.<sup>[23]</sup> Depending on the electrolyte composition (i.e., solvent and supporting electrolyte type) and used substrate, different local surroundings of the elemental Si domains can be electrochemically formed. This opens a potentially large window for adjusting the structural stability and electrochemical performance of the Si-based material.

In our previous works, we found that due to the integrated extra components, the viscoelasticity of the electrodeposited Si-based layer is substantially increased.<sup>[20–22]</sup> This effect plays a positive role for achieving an improved cycling stability of the deposits in electrolytes for LIBs.<sup>[19,20]</sup> Related to the advanced application of the Si–O–C material, our particular attention has been focused on the sulfolane (SL)-based electrolytes as electrochemically stable, low-cost, and environmentally friendly alternative to the conventional organic solvent-based ones.<sup>[20,21,24]</sup> Furthermore, SL electrolytes have the potential to substitute the broadly used room-temperature ionic liquids for deposition of refractory metals and other active elements that are impossible to deposit from aqueous electrolytes. The Si–O–C material electrodeposited from SL displays an enhanced electrochemical–mechanical stability upon lithiation, which can be ascribed to effects of the chemical composition.<sup>[20,21]</sup>

In this work, we explore the sodiation behavior of potentiostatically deposited from SL electrolyte binder- and conductive

additive-free Si–O–C composite. The quantity and the physical properties of the Si–O–C layers are studied by electrochemical quartz crystal microbalance (EQCM) with damping monitoring. By means of a combined electrochemical and spectroscopic approach, the structural aspects of the reversible sodiation of this material have been revealed. The possibility to explore the electrochemical behavior of conducting additive- and binder-free thin Si–O–C layers in Na-ion electrolyte offers an additional advantage. Since the conductive additive (e.g., super P or carbon black [CB]) displays a marked redox activity in the same potential range like Si materials,<sup>[25]</sup> our characterization approach provides opportunity to study the individual electrochemical properties of the Si–O–C material.

## 2. Results and Discussion

### 2.1. Electrochemical Deposition, Morphological, and Microgravimetric Characterization

Silicon layers were deposited electrochemically from SL-based electrolyte under potentiostatic conditions. The deposition process was monitored by EQCM to determine the mass of the deposited material.

The high sensitivity of the QCM microgravimetry ( $S = 3.78 \text{ g cm}^{-2} \text{ Hz}^{-1}$ )<sup>[26]</sup> generally permits an accurate in situ mass determination of physically or (electro)chemically deposited thin films of different nature. Typically, when the layer is rigid and smooth, its deposition triggers a linear decrease of the resonance frequency,  $f$ , which can be transformed to the corresponding mass loading,  $\Delta m$  by applying the Sauerbrey equation, Equation (1).<sup>[27]</sup>

$$\Delta f = -\frac{2f_0^2 \Delta m}{Z_{M,Q} A} = -C_{SB} \frac{\Delta m}{A} \quad (1)$$

$$\Delta f^* = f - f_0 + i \frac{(w - w_0)}{2} = \Delta f + i \frac{\Delta w}{2} \quad (2)$$

$$Z_M^* = \frac{\pi Z_Q}{i f_{0,1}} \Delta f^* \quad (3)$$

However, due to layer properties such as an increased viscoelasticity, and pronounced surface roughness and additionally influenced by the high electrolyte viscosity, the conditions for the application of Equation 1 are often not fulfilled. In either of these cases, considerable dissipative effects of the resonator oscillation can be expected. Theoretically, these effects contribute to the complex frequency shift,  $\Delta f^*$  and increase the mechanical impedance of the loaded resonator,  $Z_M^*$  Equation (2) and (3).<sup>[28–31]</sup> Therefore, to determine accurately the mass of the layer, the magnitude of the corresponding dissipative effects quantified by Equation (2) and (3) has to be analyzed as well.

In Equation (1)–(3),  $\Delta f$  is the frequency change during the deposition,  $f_0$  is the frequency of the unloaded quartz crystal,  $\Delta m$  is the mass change,  $Z_{M,Q}$  is the mechanical impedance of the quartz ( $8.849 \times 10^6 \text{ kg m}^{-2} \text{ s}^{-1}$  for a 10 MHz, AT-cut quartz),  $A$  is the mass sensitive electrode area,  $C_{SB}$  is the Sauerbrey constant ( $226.01 \text{ Hz cm}^2 \mu\text{g}^{-1}$ ),  $w$  and  $w_0$  are the damping of the loaded and unloaded quartz crystal, respectively, and  $i = \sqrt{-1}$ .

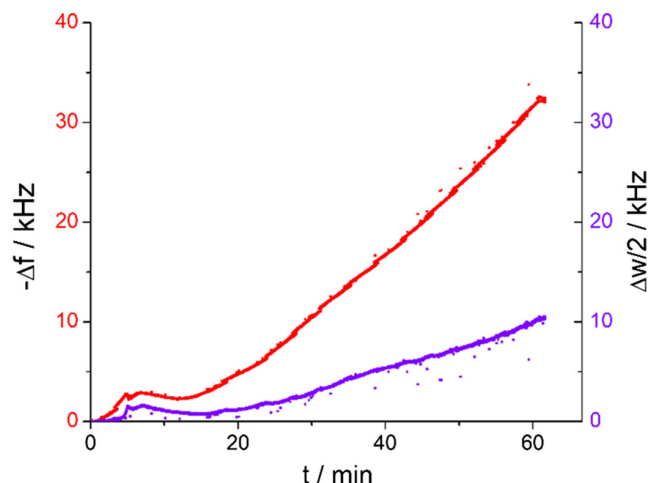


**Figure 1.** Frequency and damping changes of Cu-coated quartz piezoelectric resonator during Si–O–C deposition.

The frequency change and damping signals recorded during the deposition are plotted in **Figure 1**. The corresponding potentiostatic deposition curves can be found in Figure S1, Supporting Information. Figure 1 reveals a common trend in the resonance frequency behavior. Both parameter, frequency change and damping show a gradual increase during the entire deposition span, with the damping signal being three times lower. The detected initial frequency maximum followed by a slight decrease in a  $\Delta f$  (5–15 min) was frequently noticed in our experiments. We have attributed this phenomenon to a possible detachment of unstably adherent particles from the electrode surface at the initial stages of deposition.<sup>[21,22]</sup> The observed considerable resonance damping in electrolyte during the deposition points out that viscoelastic behavior and/or rough surface morphology of the deposit dissipate the quartz crystal oscillation, which additionally reduces the accuracy of the resonance frequency determination. Furthermore, it was already shown that electrolyte, trapped in the interfacial nano cavities, surface corrugations, and pores can act as a rigid mass, artificially elevating the amount of the deposited material, in situ detected in electrolyte media. According to Schumacher et al.,<sup>[32,33]</sup> this effect takes place when the lateral dimensions of the surface roughness are considerably smaller than the decay length  $\delta$  of the shear wave in the liquid, according to Equation (4).

$$\delta = \left( \frac{\eta}{\pi \rho f_0} \right)^{1/2} \quad (4)$$

where  $\eta_L$  is the viscosity of the solution, and  $\rho$  its density. For the SL electrolyte, used for the Si deposition at 298 K, one obtains  $\delta = 500$  nm.<sup>[21]</sup> Therefore, the electrolyte, trapped in surface cavities with dimension under this limit, will cause a Sauerbrey-like frequency shift, characteristic for a rigid layer.<sup>[31]</sup> However, this quantification will not correspond to the mass of the deposited Si–O–C layer.

To analyze completely the impact of the surface morphology, scanning electron microscope (SEM) imaging of the samples after deposition was performed. The SEM micrographs of the

deposits taken at different magnifications are shown in **Figure 2**. Surface roughness of the layers in the micrometer range is clearly detectable at low magnifications (Figure 2a,b,e,f), which definitely exceeds the lateral roughness limit of  $\delta = 500$  nm and therefore, cannot be interpreted by applying Schumacher's model, describing only the effect of small roughness. Additionally, at high magnifications (Figure 2c,d,g,h) open pores and surface corrugations at the nanoscale are clearly visible. This type of porosity is much more pronounced for longer deposition times (Figure 2g,h) suggesting that the electrolyte trapped in these cavities will display Sauerbrey-like microgravimetric behavior.

Theoretical estimation of the roughness-dependent dissipative phenomena according to the advanced multiscale roughness model developed by Urbakh and Daikhin suggests a complex nonlinear behavior of the damping and frequency, depending on two geometric parameters (lateral and vertical).<sup>[21,34–36]</sup> The experimentally obtained damping observed at the end of the deposition period conforms very well with the theoretically predicted values corresponding to these roughness parameters.<sup>[21]</sup>

Next to the surface roughness, the second major contribution to the dissipation of the resonator oscillation is the viscoelastic mechanical behavior of the layer. This effect can be accounted by modeling the mechanical shear impedance of the layer, which directly depend on thickness,  $h$ , density,  $\rho$ , frequency,  $\omega$ , and complex shear modulus of the layer,  $G^*$ , Equation (5).<sup>[22,31,37]</sup>

$$Z_{m,s}^*(h) = j\sqrt{\rho G^*} \tan \sqrt{\rho/G^*} \omega h \quad (5)$$

For a thin rigid layer,  $\sqrt{\rho/G^*} \rightarrow 0$ ,  $\tan \sqrt{\rho/G^*} \rightarrow \sqrt{\rho/G^*}$ , and finally  $Z_{m,s}^*(h) = j\rho\omega h$ . Therefore, substitution of the last expression for  $Z_{m,s}^*$  in Equation (3) under the condition of smooth and rigid layer leads to the well-known Sauerbrey relation (Equation (1)).

Additionally, the contact with a liquid phase can analogously impede the oscillation of the quartz resonator due to the liquid viscosity. For example, in the case of infinite Newtonian liquid  $G^* = j\omega\eta$ ,  $\tan \sqrt{\rho/G^*} \rightarrow 1$ , and  $Z_{m,s}^* = \sqrt{j\rho\omega\eta}$ .

Clearly, the surface roughness and the mechanical properties of the layer have a mutual impact on the resonance frequency. On the one hand, the existence of small roughness and the trapped electrolyte cannot be separated in a liquid phase from the Sauerbrey-related frequency shift and on the other hand, the strong roughness induces a high dissipation of the resonator oscillation. These effects, together with the viscoelasticity, insert a high inaccuracy when in situ EQCM approach is applied for quantification of the electrodeposited Si–O–C mass and therefore, have to be minimized or circumvented.

For precise evaluation of the specific capacity, washing of the layers with solvent and subsequent drying are necessary. This can also enable us to remove completely the electrolyte used for the deposition and to eliminate the entrapped liquid media, including those components of the Si–O–C deposit that are loosely bound and/or volatile. Therefore, to determine only the mass of the stably attached layer, QCM experiments were performed in argon atmosphere after washing and continuous overnight drying (of the layer) under vacuum. The resulting damping, measured during the experiment in argon atmosphere,

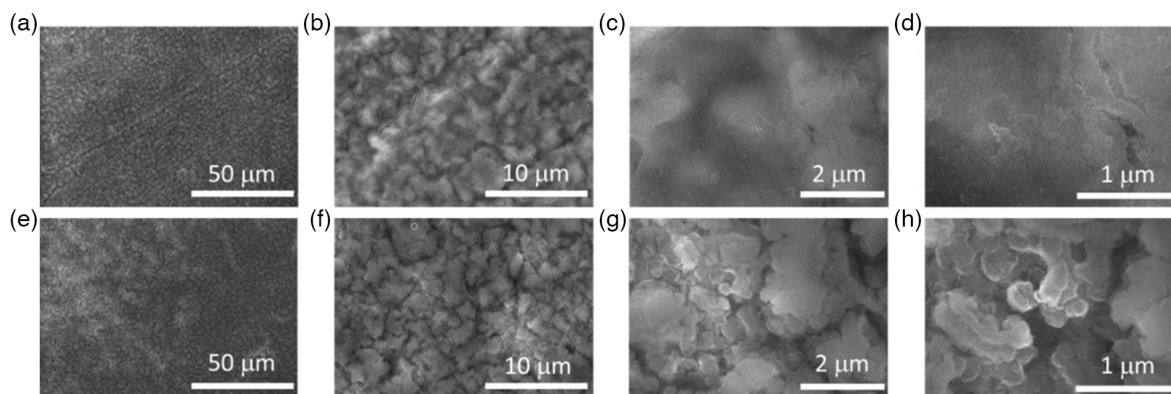


**Figure 2.** Scanning electron microscope (SEM) images of the Si–O–C layers deposited a–d) for 1 h and e–h) for 2 h taken at four different magnifications.

was minimal, only 2.7% from the frequency change, compared to 30% for the measurements in electrolyte media, demonstrating that the observed in liquid media dissipative effects can be minimized to the greatest possible degree. Thus, the estimated dissipation term  $\frac{\Delta W}{2}$  (Equation (2)) is in the case of measurements in argon atmosphere negligible and therefore Equation (1) can be applied to determine the mass of the Si–O–C material (Figure (3)). The procedure of weight evaluation of the samples is described in Supporting Information.

## 2.2. Sodiation Behavior of the Electrodeposited Si–O–C Layers

To characterize the redox activity of the Si–O–C material in Na-ion electrolyte, galvanostatic charge–discharge measurements were performed in broad potential limits (0.01–2.0 V) at low current density (Figure 4a). The obtained chronopotentiometric profiles were transformed in differential capacity (DC) plots (Figure 4b,c). Cyclic voltammetry in a broader potential range (0.01–3.0 V) is additionally presented in Supporting Information (Figure S4, Supporting Information). It was indicated that the DC approach for electrochemical analysis offers certain advantages in comparison to cyclic voltammetry. In view

of this, Palagonia et al.<sup>[38]</sup> compared the applicability of both methods for characterization of energy storage materials and concluded that the distortion of the peak signal due to ohmic resistance, typical for cyclic voltammetry, can introduce difficulties in voltammetric interpretation. This problem can be overcome by transforming the galvanostatic cycling with potential limitation (GCPL) curves to DC signal. The approach is particularly useful in the case of electrodeposited Si–O–C layers, where no conductive additive is present in the material. Furthermore, since GCPL and DC present graphically one and the same measurement, the DC approach offers the possibility for a more straightforward, qualitative and battery-relevant interpretation than the CV.<sup>[38]</sup>

The constant current sodiation–desodiation experiment demonstrates a sloped potential profile (Figure 4a) typical for the Si-based materials.<sup>[10,16]</sup> The first galvanostatic charge shows 1500 mAh g<sup>−1</sup> specific capacity, which drops significantly in the next cycles and stabilizes at around 500 mAh g<sup>−1</sup>, confirming 66% irreversible capacity. The initial cathodic DC potential profile indicates redox activity in the potential range 1–0 V, attributed to sodiation of the Si–O–C material and to the formation of the SEI layer, accelerated by the presence of fluorinated ethylene carbonate (FEC) additive. The subsequent second and third cathodic DC curves display electroactivity in the same potential region, however, lower DCs were observed. This suggests an effective formation of SEI and/or irreversible material loss during the first charge–discharge cycle. The anodic DC curves showed a reproducible and to higher potentials extended redox activity due to significant ohmic resistance during desodiation of the material. There are two distinguished potential regions, 0–0.7 V displaying a visible shoulder, overlapping with a peak, extended to higher potentials up to 2 V versus Na/Na<sup>+</sup>. Several reports in the literature discuss the sodiation behavior of Si-based materials.<sup>[10,12–16]</sup> Nevertheless, since the conductive additive (e.g., CB) displays a specific pronounced redox activity in sodium-ion electrolytes, overlapping with that of Si material, the individual electrochemical behavior of the latter is underexplored.

The lithiation performance of identically deposited Si–O–C composite layers has been studied in our previous work.<sup>[20]</sup> In contrast to the sodiation, in Li-ion electrolyte, the material displayed much higher reversible capacity (850 mAh g<sup>−1</sup> after

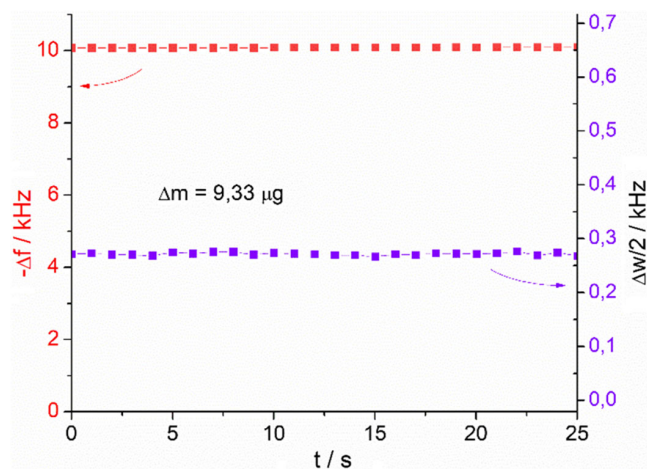


**Figure 3.** Frequency change and damping measured after Si–O–C deposition, recorded in argon after washing and drying of the layer.

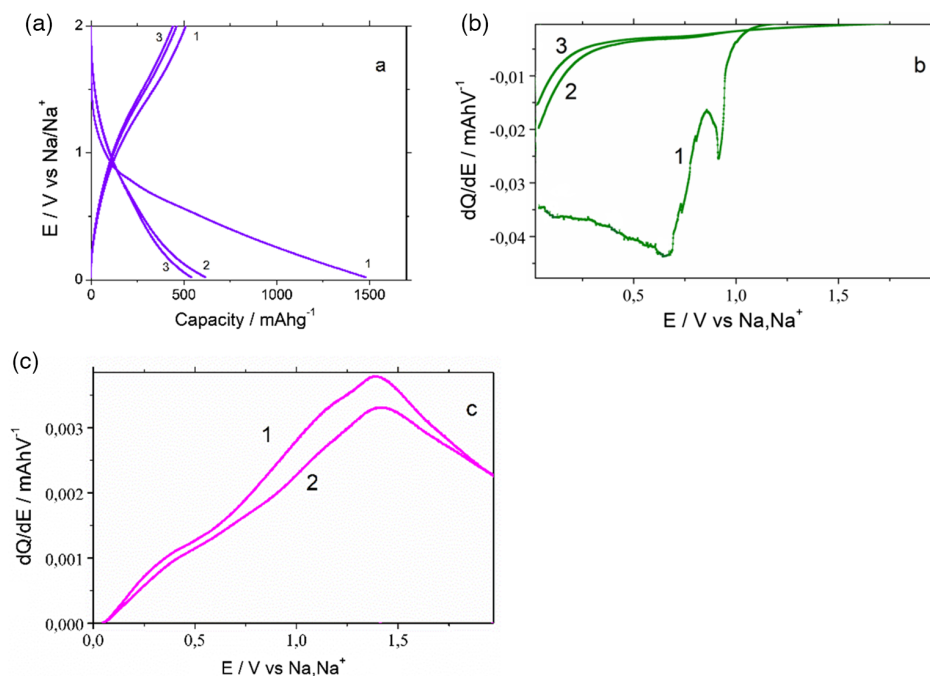


**Figure 4.** Constant current potential profiles of a) Si–O–C composite layer and corresponding b) cathodic and c) anodic differential capacity curves.  $j = 0.07 \text{ Ag}^{-1}$ .

250 cycles) and reversible redox activity in the characteristic for Si potential range. The observed differences in the capacities in both electrolytes conform with the contrast in the ionic radii of Li and Na, and this effect is supported by other studies.<sup>[3–5]</sup>

### 2.3. Chemical Composition of Si–O–C Layers and Impact of Electrochemical Sodiation

The surface chemical composition of pristine, sodiated, and desodiated Si–O–C layers was analyzed by X-Ray photoelectron spectroscopy (XPS) and the results were compared. **Figure 5** shows the corresponding core-level XPS spectra of Si2p and C1s. Survey photoelectron spectra for the three samples are presented in Figure S4, Supporting Information.

The Si2p core-level spectrum of the as-deposited layer is presented in Figure 5a. The spectrum demonstrates a visible peak at  $\text{BE} = 99.2 \text{ eV}$ , characteristic for the Si2p<sub>3/2</sub> component of elemental silicon (Si<sup>0</sup>).<sup>[39,40]</sup> According to our fit procedure, which excludes BE position constraints, the additional Si2p components appear at 102.2 and 96.1 eV for Si2p<sub>3/2</sub> core-level peaks. The small component at 96.1 eV was necessary to fully interpret the shape of the Si2p spectrum of the pristine material. The fitted component at 102.2 eV can be attributed to Si embedded in the inorganic matrix and surrounded predominantly by carbon and oxygen atoms in different stoichiometric ratios (Si<sub>x</sub>C<sub>y</sub>O<sub>z</sub>), as already indicated by Link et al. and Coupé et al.<sup>[21,41]</sup> Additionally, previous study on SiC composite materials has reported that Si2p XPS peaks ranging from 100 eV (SiC<sub>4</sub> groups) to  $\approx 103 \text{ eV}$  (SiO<sub>4</sub>) can be expected.<sup>[42]</sup> Other published research on silicon oxycarbide material reveals predominantly SiO<sub>3</sub>C and SiO<sub>4</sub> groups.<sup>[12]</sup>

The total elemental composition of the layer before electrochemical sodiation involves 41.7% Si, 29.2% C, 22.9% O, and traces of N, Cl, and S each less than 1% (Table S1, Supporting Information).

After electrochemical sodiation the Si present in both phases converts to intermediate redox states, average low and high, Si<sup>int1</sup> at 100 eV and Si<sup>int2</sup> at 102.6 eV, respectively (Figure 5b). This process involves integration of Na ions into the close surrounding of carbon, oxygen, and silicon species, where two different structural domains of Si coexist. We anticipate that the Si–O–C composite layer remains intact after the electrochemical experiment since signal from the Cu substrate was not detected by XPS in the sodiated and desodiated samples. Hence, the major amount of Si should be irreversibly oxidized, however, remaining integrated in the layer structure.

The deconvoluted spectra of the desodiated material reveal the following features. First, the binding energy (BE) position of Si<sup>int1</sup> (BE = 100 eV) does not shift, which is probably related to the chemical inertness of these type of species. Second, the peak at 102 eV (associated with Si<sup>int2</sup>) shifts to the higher BE position, from 102.6 to 103.0 eV. This points to a reversible redox process where the Si<sup>int2</sup> component is involved, which could be associated with the separation of the Na ions from the local surrounding of Si upon desodiation. Similar effect related to the Si2p<sub>3/2</sub> core level in the BE range 101–104 eV was discussed by Dou et al. as characteristic for the sodiation behavior of the silicon oxycarbide composite.<sup>[16]</sup>

Deconvolution of the C1s spectra (Figure 5d–f) reveals carbon atoms in three different environments. The most intensive C1s peaks at 285 eV are assigned to C–C/H fragments. The C1s signal at 287.2 eV has been attributed to carbon in

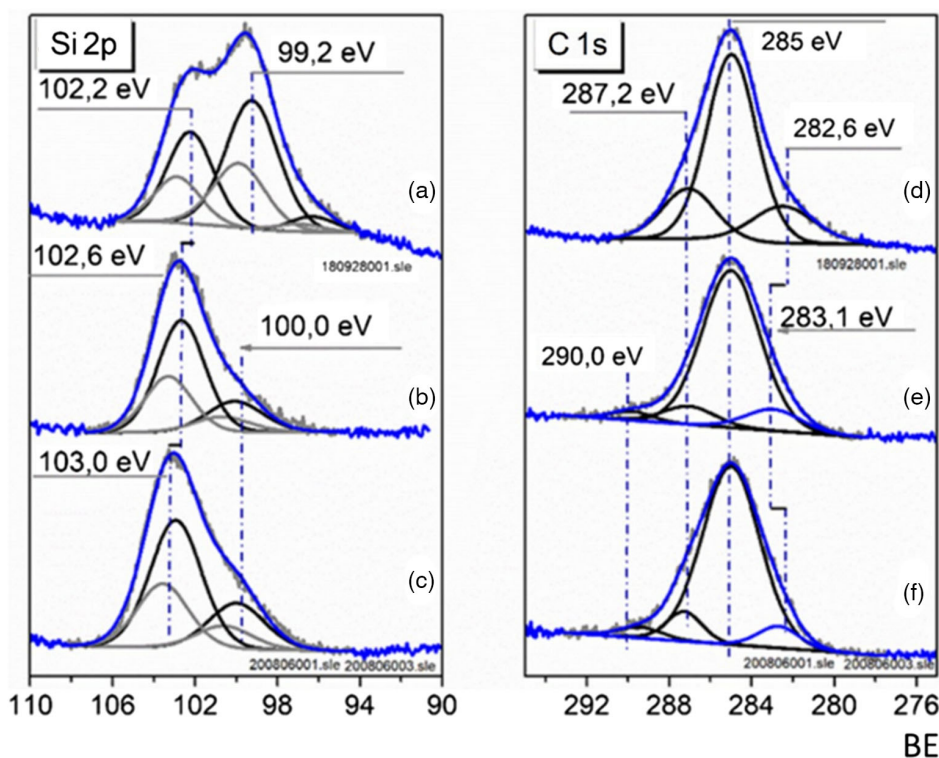


**Figure 5.** Si2p and C1s core-level a,d) peaks of pristine, b,e) sodiated, and c,f) de-sodiated material, respectively. The experimental spectra are shown in light grey, the envelope peak is colored in blue, the fitted components are in black, and the Si2p<sub>1/2</sub> core levels are in grey.

–C–O– group.<sup>[20,21]</sup> The peaks at higher BE detected in the range 289.7–290.0 eV are often discussed as contributions of R'(R'') C=O, R'(O)C–O, –CO<sup>–</sup><sub>3</sub>, or CHF (fluoroform moiety)–containing species, typically deposited on the electrode surface as a result of solid electrolyte interphase (SEI) formation.<sup>[43]</sup> Additionally, a weak component at around 282–283 eV present in all spectra points out to the formation of silicon carbide (i.e., Si–C bond)<sup>[44]</sup> and sodiated carbon species.<sup>[16,45]</sup> A closer look at the BE position of this component shows that upon sodiation its BE shifts to higher values (283.1 eV) and after desodiation it returns to the original position. This indicates an electrochemical activity of carbon, as a building element of the Si–O–C layers, in sodium-ion electrolytes.

The XPS analysis suggests that three different possible processes can be involved in the reversible energy storage in Si–O–C material: 1) insertion/de-insertion of Na<sup>+</sup> into the closed Si surrounding (Si<sub>x</sub>O<sub>y</sub>C<sub>z</sub>), accompanied by change in the intermediate redox states of Si; 2) insertion/de-insertion of Na<sup>+</sup> in the individual carbon phase of the composite; and 3) reversible sodiation of SiC.

However, as discussed by Dou et al.,<sup>[16]</sup> the formation of larger amounts of SiC can be excluded, since this process should be linked to a presence of Si 2p component at 100 eV. Furthermore, Na–Si alloy formation can be ruled out as there is no peak at about 99 eV in the Si 2p spectra.

## 2.4. Galvanostatic Performance and Rate Capability Tests

To test the rate capability and the long-term cycling performance of the materials, galvanostatic electrochemical experiments with

the Si–O–C layers were performed at different constant currents in the potential limits 0.02–2.8 V (Figure 6a,b). The results showed a good electrochemical stability and the typical characteristics of a silicon-based material, described in Section 2.3. It can be further seen that at low and moderate current densities ( $j \leq 150 \text{ mA g}^{-1}$ ), the material displays high capacities in the range of 600–700 mAh g<sup>–1</sup> (Figure 6a). At higher cycling currents ( $6 \text{ A g}^{-1} \leq j \leq 150 \text{ mA g}^{-1}$ ), the SiOC layer still preserves decent discharge capacity values (300–450 mAh g<sup>–1</sup>).

The enhanced cycling behavior (i.e., outstanding electrochemical stability and sufficient capacity at high cycling currents) is related to the specific structural properties of the Si–O–C layers that tolerate accelerated sodium-ion transport and prevent the mechanical breakdown of the redox active material. It can be suggested that the main role for achieving these superior functional properties and stable electrochemical behavior has the electrolyte composition used for the deposition. The approach of using SL-based electrolyte enables integration of buffering components (non-Si including species) in the deposited layer, enabling the desired mechanical stabilization of the material. In our earlier works, we have observed comparable stabilization effect of the Si–O–C layers, triggered by incorporation of contaminants, in Li-ion electrolytes.<sup>[19,20]</sup>

The galvanostatic performance of the Si–O–C layers studied in this work is compared with the behavior of different Si-, SiO-, and SiOC-based materials, available in the literature (Table 1). IRC, CR, and Coulomb efficiency (CE) have been considered as relevant for the comparison parameters. The Si–C–O material displayed similar cycling performance to the

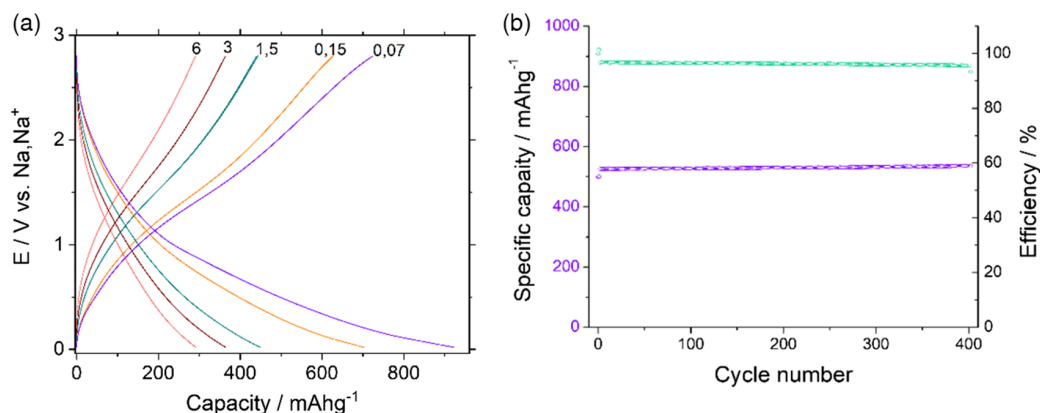


**Figure 6.** a) Charge–discharge galvanostatic potential profiles measured at different current densities, presented above the curves in  $A\ g^{-1}$ . b) Specific discharge capacity during long-term galvanostatic cycling at  $j = 70\ mA\ g^{-1}$  in the potential range 0,02–2.2 V versus  $Na,Na^+$ .

**Table 1.** Sodiation behavior of Si-based materials. IRC—initial reversible capacity; CR—capacity retention; EC—coulombic efficiency; ICE—initial coulombic efficiency; CB—carbon black; CE—Coulomb efficiency; CB—carbon black; PVDF—polyvinylidene fluoride; CMC—carboxymethyl cellulose.

Si component	Electrode material	IRC	CR	CE (ICE)	References
Si powder	Active material, CB and polyamic acid–65:21:4	No reversible capacity	–	–	[7]
Si nanoparticles	Active material, CMC, and Super P—50:30:20	279 $mAh\ g^{-1}$ (20 $mA\ g^{-1}$ )	248 $mA\ g^{-1}$ after 100 cycles (20 $mA\ g^{-1}$ )	98% ( $\approx 26\%$ )	[10]
Crystalline silicon (c-Si)	Active material, sodium alginate, CB—70:10:20	<50 $mAh\ g^{-1}$ , (c-Si)	255 $mAh\ g^{-1}$ after 50 cycles at (100 $mA\ g^{-1}$ ) a-Si	$\approx 97\%$ ( $\approx 40\%$ ) a-Si	–
Amorphous silicon (a-Si)		283 $mAh\ g^{-1}$ , (a-Si)			
Crystalline silicon (c-Si)	Active material, sodium alginate, Super P—60:10:30	7.5 $mAh\ g^{-1}$ (c-Si)	150 $mAh\ g^{-1}$ over 100 cycles	–	[13]
Amorphous silicon (a-Si)		72 $mAh\ g^{-1}$ (a-Si)	100 cycles		
Silicon oxide (SiO)		74 $mAh\ g^{-1}$ (SiO)	(36 $mA\ g^{-1}$ ) (a-Si)		
SiO powder, granular silicon monoxide (SiO)	Pure active material	220 $mAh\ g^{-1}$ (50 $mA\ g^{-1}$ )	170 mA h at the 100th cycle (50 $mA\ g^{-1}$ )	93% (37–55%)	[11]
Si/SiO <sub>2</sub> -ordered-mesoporous-carbon	Active material, CB, and PVDF—70:20:10	550 $mAh\ g^{-1}$ (50 $mA\ g^{-1}$ )	423 $mAh\ g^{-1}$ over 100 cycles (50 $mA\ g^{-1}$ ) 190 $mAh\ g^{-1}$ over 500 cycles (1000 $mA\ g^{-1}$ )	$\geq 95\%$ ( $\approx 50\%$ )	[15]
Submicron-sized silicon oxycarbide	Active material, CB and PVDF—80:10:10	188 $mAh\ g^{-1}$ (25 $mA\ g^{-1}$ )	150 $mAh\ g^{-1}$ after 40 cycles (25 $mA\ g^{-1}$ )	99% (30–47%)	[12]
Silicon oxycarbide (SiOC)	Active material, Super C65, CMC—80:10:10	128 $mAh\ g^{-1}$ (SiOC)	100 $mAh\ g^{-1}$ after 500 cycles, (SiOC)	98.4% (SiOC)	[16]
HF-etched Silicon oxycarbide (SiOC–HF)		169 $mAh\ g^{-1}$ (SiOC–HF) (20 $mA\ g^{-1}$ )	after 500 cycles, (SiOC) (20 $mA\ g^{-1}$ )	94.7% (SiOC–HF) (37%)	
SiOC powder	Active material, acetylene black, PVDF—70:10:20	189 $mAh\ g^{-1}$ (25 $mA\ g^{-1}$ )	160 $mAh\ g^{-1}$ for 200 cycles (25 $mA\ g^{-1}$ )	$\approx 99\%$ ( $\approx 45\%$ )	[14]
Electrodeposited Si–O–C composite	Pure active material	509 $mAh\ g^{-1}$ ( $E_a = 2\ V$ ) 722 $mAh\ g^{-1}$ ( $E_a = 2,8\ V$ ) (70 $mA\ g^{-1}$ )	540 $mAh\ g^{-1}$ for 400 cycles (150 $mA\ g^{-1}$ )	$\geq 97.0\%$ (34%)	This work

Si/SiO<sub>2</sub>-ordered-mesoporous-carbon composite<sup>[15]</sup> and superior electrochemical behavior (IRC and CR) than the rest of the listed materials. As for many types of Si-based materials,<sup>[10,12,14,16]</sup> the initial Coulomb efficiency (ICE) was low (about

34% at first cycle) and increased further with the cycle number to steady-state values at  $\geq 97.0\%$  that are comparable to other materials. The low ICE value of our material can be attributed to the mutual impact of SEI formation, and the irreversible oxidation of

the initially deposited elemental Si<sup>0</sup> phase (see Section 2.3). It is worth noting that the presence of conductive additives (up to 30%) can considerably influence the discussed performance parameters of the SIB anodes (Table 1) and this factor is not assessed systematically by the present comparison.

### 3. Conclusion

Thin Si–O–C composite layers were deposited electrochemically under potentiostatic conditions from SL-based organic electrolyte. The application of QCM technique with dissipation monitoring enabled a precise evaluation of the layer growth and its physical properties. The main factors that introduce inaccuracy of the layer mass determination (surface roughness, viscoelasticity, and trapped electrolyte) were circumvented by QCM measurements of dry Si–O–C layers in Ar atmosphere. The material showed a promising sodiation–desodiation performance in terms of specific capacity, rate capability, and long-term electrochemical stability. The Si–O–C anodes delivered a high IRC (722 mAh g<sup>-1</sup>, E<sub>a</sub> = 2.8 V, and j = 70 mA g<sup>-1</sup>) and preserved a long-term capacity of 540 mAh g<sup>-1</sup> for at least 400 galvanostatic cycles at j = 150 mA g<sup>-1</sup>. The XPS analysis indicated that the reversible electroactivity of the material in sodium-ion electrolyte is attributable to the complex contribution of carbon and silicon redox centers. The preserved stable performance of the Si–O–C layers can be ascribed to their improved mechanical stability and accelerated sodium-ion transport in the porous anode structure.

### 4. Experimental Section

**Chemicals and Materials:** SL, diethyl carbonate (DEC), ethylene carbonate (EC), FEC, and hexane with 99% purity, respectively, and analytical grade silicon tetrachloride were purchased from Alfa Aesar. Tetrabutylammonium chloride (TBACl, ≥97% purity), sodium bis(trifluoromethanesulfonyl)imide (NaTFSI), and sodium metal were provided by Sigma-Aldrich.

SL was dried under vacuum at 60 °C to a moisture level of <20 ppm, which corresponds to a molar concentration <0.9 mM. Karl–Fischer titration (Metrohm 831 KF coulometer) was used to monitor the water contamination in the solutions. The 0.1 M TBACl was added as supporting electrolyte to the solvent and the solution was dried again for additional 2 days with a molecular sieve (pore diameter 0.3 nm, Carl Roth, Germany) to a water content of <20 ppm. The 0.5 M SiCl<sub>4</sub> served as a precursor for Si electrodeposition.

**Electrochemical Experiments:** All electrodeposition experiments were performed potentiostatically at room temperature (25 °C) in an argon-filled glove box (MBraun UNIlab LMF auto) with O<sub>2</sub> and H<sub>2</sub>O contents below 0.1 ppm. QCM measurements and potentiostatic deposition were carried out in an in-lab-made PTFE cell, using a multichannel potentiostat (VMP3) from Bio-Logic Scientific Instruments. The silicon layers were electrodeposited from 0.5 M SiCl<sub>4</sub>, 0.1 M TBACl in SL. Si deposition was performed in three-electrode arrangement, consisting of Cu as working electrodes, a large 2 × 2 cm<sup>2</sup> Pt sheet as counter electrode, and in-lab-made Ag/AgCl reference electrode for organic media.<sup>[24,46]</sup> Electrolyte solution—containing 0.1 M TBACl in SL was used for the preparation of the reference electrode.<sup>[24]</sup>

Prior to the experiments, the copper substrates were mirror-polished with a diamond paste (1 μm), sonicated for 5 min in ethanol, rinsed with acetone, and dried in argon atmosphere for 20 min. The electrodes were clamped to the cell via an O-ring. The Pt plate was heated to red glow before each measurement.

Immediately after deposition, the samples were washed with organic solvent.

The samples were electrochemically characterized in 1 M NaTFSI, EC: DEC, and 3% FEC electrolyte in coin cells (CR2016) against Na metal foil. Na metal was used as a reference electrode for the cyclic voltammetry and EQCM.

**EQCM and Evaluation of Electro-Gravimetric Data:** AT-cut quartz oscillators, provided by Vectron International, with a resonance frequency f<sub>0</sub> = 10 MHz were used for the QCM measurements. The bare quartz plates were coated by thermal evaporation, first with a Cr-adhesive layer (d = 10 nm), followed by a Cu layer (d = 200 nm). Saunders 250B Network Analyzer Peripheral Component Interconnect computer card (Saunders and Associates Inc.) equipped with an in-lab-written software was used for monitoring the admittance of the quartz resonator.

Both metallic contacts of the resonator were coupled with the network analyzer to measure the electrical parameters of the quartz in the frequency range around the resonance value and additionally, the top contact was connected to the VMP3 potentiostat as working electrode for the electrodeposition of silicon. With this setup, it was possible to monitor in operando the change of frequency and to extract the damping from the resonance curve. To this end, the real part of the admittance was online fit during the whole experiment with a Lorentzian curve. Thus, the resonance frequency at the admittance maximum, f, and the damping parameter ω (full width at half height) were recorded as output parameters.

**X-Ray Photoelectron Spectroscopy and SEM:** X-Ray photoelectron spectroscopy (XPS) analyses were carried out with a Specs SAGE spectrometer (base pressure <1 × 10<sup>-8</sup> mbar) equipped with a Phoibos 150 electron analyzer using a focused monochromatized AlKα radiation (hν = 1486.7 eV). The measurements were performed using analyzer pass energies of 50 eV for survey spectra and 13 eV for high-resolution spectra. This operation conditions led to a total energy resolution of 0.6 eV (full width at half maximum of Ag 3d5/2 at pass energy of 13 eV of sputtered Ag reference sample). All XPS spectra were recorded at normal emission (Θ = 0°, the angle between the surface normal and the leaving electrons). The absolute error in the acquisition of BEs was 0.1 eV, as quoted by the instrument manufacturer (SPECS Surface Nano Analysis GmbH, Germany).

The core level spectra were analyzed by subtracting a Shirley-type background<sup>[47]</sup> and fitted by a weighed least-square fitting model (70% Gaussian, 30% Lorentzian) using the software package CASA XPS (Version 23.16 Dev52, Casa Software Ltd.). Samples were not sputtered to avoid undesirable interaction between the silicon and Ar<sup>+</sup>.<sup>[48–50]</sup> The spectra were normalized according to the BE of C1s peak at 285.0 eV caused by the C–C/H moieties from electrolyte components.

After sample preparation and washing (in a glove box under argon atmosphere), the samples were packed into a hermetically sealed transfer box for transportation into the fast entry lock chamber. To prevent the samples from moisture/air exposure, a nitrogen dry-box (Carl Roth GmbH, Germany) was mounted to the XPS spectrometer so that the samples could be easily removed from the transfer-box within the dry-box, placed into the transfer chamber and measured under pressure of 5 × 10<sup>-8</sup> mbar.

Ultrahigh resolution field-emission SEM (FE-SEM), Hitachi S-4800, was used for the morphological characterization of the Si layers.

### Supporting Information

Supporting Information is available from the Wiley Online Library or from the author.

### Acknowledgements

Support by the Center of Micro- and Nanotechnologies (ZMN) (DFG Resources reference: RI\_00009), a DFG-funded core facility (Grant nos. MU 3171/2-1 + 6-1, SCHA 632/19-1 + 27-1, HO 2284/4-1 + 12-1) of the TU Ilmenau, is gratefully acknowledged. The authors are thankful for the research funding by the state of Thuringia and the European



Union within the frame of the European Funds for Regional Development (EFRD) under grant no. 12021–715.

Open Access funding enabled and organized by Projekt DEAL.

## Conflict of Interest

The authors declare no conflict of interest.

## Data Availability Statement

The data that support the findings of this study are available in the supplementary material of this article.

## Keywords

electrodeposition, silicon, sodium-ion batteries, sulfolane

Received: December 30, 2021

Revised: February 5, 2022

Published online: March 25, 2022

- [1] P. Greim, A. A. Solomon, C. Breyer, *Nat. Commun.* **2020**, *11*, 4570.
- [2] J.-Y. Hwang, S.-T. Myung, Y.-K. Sun, *Chem. Soc. Rev.* **2017**, *46*, 3529.
- [3] K.M. Abraham, *ACS Energy Lett.* **2020**, *5*, 3544.
- [4] S. C. Jung, D. S. Jung, J. W. Choi, Y.-K. Han, *J. Phys. Chem. Lett.* **2014**, *5*, 1283.
- [5] C.-Y. Chou, M. Lee, G. S. Hwang, *J. Phys. Chem. C* **2015**, *119*, 14843.
- [6] S. Komaba, Y. Matsuura, T. Ishikawa, N. Yabuuchi, W. Murata, S. Kuze, *Electrochem. Commun.* **2012**, *21*, 65.
- [7] L. D. Ellis, B. N. Wilkes, T. D. Hatchard, M. N. Obrovac, *J. Electrochem. Soc.* **2014**, *161*, A416.
- [8] S. Huang, L. Liu, Y. Zheng, Y. Wang, D. Kong, Y. Zhang, Y. Shi, L. Zhang, O. G. Schmidt, H. Y. Yang, *Adv. Mater.* **2018**, *30*, 1706637.
- [9] S.-M. Zheng, Y.-R. Tian, Y.-X. Liu, S. Wang, C.-Q. Hu, B. Wang, K.-M. Wang, *Rare Met.* **2021**, *40*, 272.
- [10] Y. Xu, E. Swaans, S. Basak, H. W. Zandbergen, D. M. Borsa, F. M. Mulder, *Adv. Energy Mater.* **2016**, *6*, 1501436.
- [11] M. Shimizu, H. Usui, K. Fujiwara, K. Yamane, H. Sakaguchi, *J. Alloys Compd.* **2015**, *640*, 440.
- [12] M. Weinberger, C. Pfeifer, S. Schindler, T. Diemant, R. J. Behm, M. Wohlfahrt-Mehrens, *J. Mater. Chem. A* **2015**, *3*, 23707.
- [13] C.-H. Lim, T.-Y. Huang, P.-S. Shao, J.-H. Chien, Y.-T. Weng, H.-F. Huang, B. J. Hwang, N.-L. Wu, *Electrochim. Acta* **2016**, *211*, 265.
- [14] C. Chandra, J. Kim, *Chem. Eng. J.* **2018**, *338*, 126.
- [15] L. Zeng, R. Liu, L. Han, F. Luo, X. Chen, J. Wang, Q. Qian, Q. Chen, M. Wie, *Chem. Eur. J.* **2018**, *24*, 4841.
- [16] X. Dou, D. Buchholz, M. Weinberger, T. Diemant, M. Kaus, S. Indris, R. J. Behm, M. Wohlfahrt-Mehrens, S. Passerini, *Small Methods* **2019**, *3*, 1800177.
- [17] J. Pu, Z. Shen, C. Zhong, Q. Zhou, J. Liu, J. Zhu, H. Zhang, *Adv. Mater.* **2020**, *32*, 1903808.
- [18] T. Osaka, H. Nara, T. Momma, T. Yokoshima, *J. Mater. Chem. A* **2014**, *2*, 883.
- [19] C. A. Vlaic, S. Ivanov, R. Peipmann, A. Eisenhardt, M. Himmerlich, S. Krischok, A. Bund, *Electrochim. Acta* **2015**, *168*, 403.
- [20] S. Link, M. Kurniawan, A. Dimitrova, S. Krischok, A. Bund, S. Ivanov, *Electrochim. Acta* **2021**, *380*, 138216.
- [21] S. Link, A. Dimitrova, S. Krischok, A. Bund, S. Ivanov, *ACS Appl. Mater. Interfaces* **2020**, *12*, 57526.
- [22] S. Ivanov, C. Vlaic, A. B. I. Efimov, *Electrochim. Acta* **2016**, *219*, 251.
- [23] S. Ahn, H. Nara, T. Momma, T. Osaka, *Mater. Lett.* **2019**, *251*, 184.
- [24] S. Link, S. Ivanov, A. Dimitrova, S. Krischok, A. Bund, *Electrochem. Commun.* **2019**, *103*, 7.
- [25] C.-M. Wu, P.-I. Pan, Y.-W. Cheng, C.-P. Liu, C.-C. Chang, M. Adveev, S.-K. Lin, *J. Power Sources* **2017**, *340*, 14.
- [26] J. Hu, X. Huang, S. Xue, G. Yesilbas, A. Knoll, O. Schneider, *Electrochem. Commun.* **2020**, *116*, 106744.
- [27] G. Sauerbrey, *Z. Phys.* **1959**, *155*, 206.
- [28] S. J. Martin, G. C. Frye, A. J. Ricco, *Anal. Chem.* **1993**, *65*, 2910.
- [29] R. Lucklum, P. Hauptmann, *Sens. Actuators B* **2000**, *70*, 30.
- [30] R. Lucklum, C. Behling, P. Hauptmann, *Sens. Actuators B* **2000**, *65*, 277.
- [31] A. Bund, M. Schneider, *J. Electrochem. Soc.* **2002**, *149*, E331.
- [32] R. Schumacher, G. Borges, K. K. Kanazawa, *Surf. Sci.* **1985**, *163*, L621.
- [33] R. Schumacher, J. G. Gordon, O. Melroy, *J. Electroanal. Chem.* **1987**, *216*, 127.
- [34] M. Urbakh, L. Daikhin, *Langmuir* **1994**, *10*, 2836.
- [35] M. Urbakh, L. Daikhin, *Phys. Rev. B* **1994**, *49*, 4867.
- [36] L. Daikhin, E. Gileadi, G. Katz, V. Tsionsky, M. Urbakh, D. Zagidulin, *Anal. Chem.* **2002**, *74*, 554.
- [37] V. Granstaff, S. Martin, *J. App. Phys.* **1994**, *75*, 1319.
- [38] M. S. Palagonia, C. Erinmwingbovo, D. Brogioli, F. La Mantia, *J. Electroanal. Chem.* **2019**, *847*, 113170.
- [39] F.-Y. Lee, Z.-Z. Wu, L.-C. Kao, F.-M. Chang, S.-W. Chen, S.-K. Jangjian, H.-Y. Cheng, W.-L. Chen, Y.-M. Chang, K. Y. Lo, *Sci. Rep.* **2017**, *7*, 13022.
- [40] K. Ohishi, T. Hattori, *Jpn. J. Appl. Phys.* **1994**, *33*, L675.
- [41] T. Momma, S. Aoki, H. Nara, T. Yokoshima, T. Osaka, *Electrochem. Commun.* **2011**, *13*, 969.
- [42] A. Coupé, H. Maskrot, E. Buet, A. Renault, P. J. Fontaine, L. Chaffron, *J. Eur. Ceram. Soc.* **2012**, *32*, 3837.
- [43] F. Speck, M. Ostler, S. Besendörfer, J. Krone, M. Wanke, T. Seyller, *Ann. Phys.* **2017**, *529*, 1700046.
- [44] S. Dalavi, P. Guduru, B. L. Lucht, *J. Electrochem. Soc.* **2012**, *159*, A642.
- [45] A. Ponrouch, D. Monti, A. Boschini, B. Steen, P. Johansson, M. R. Palacin, *J. Mater. Chem. A* **2015**, *3*, 22.
- [46] A. Saheb, J. Janata, M. Josowicz, *Electroanalysis* **2006**, *18*, 405.
- [47] D. A. Shirley, *Phys. Rev. B* **1972**, *5*, 4709.
- [48] J. S. Pan, A. T. S. Wee, C. H. A. Huan, H. S. Tan, K. L. Tan, *J. Appl. Phys.* **1996**, *79*, 2934.
- [49] T. Bekkay, E. Sacher, A. Yelon, *Surf. Sci.* **1989**, *217*, L377.
- [50] B. Lamontagne, E. Sacher, M. R. Wertheimer, *Appl. Surf. Sci.* **1991**, *52*, 71.